

# **Implementing Reactivity in Molecular Dynamics Simulations with the Interface Force Field (IFF-R) and Other Harmonic Force Fields**

by

Jordan J. Winetrout<sup>1,2</sup>, Krishan Kanhaiya<sup>1</sup>, Geeta Sachdeva<sup>3</sup>, Ravindra Pandey<sup>3</sup>, Behzad Damirchi<sup>4</sup>, Adri van Duin<sup>4</sup>, Gregory Odegard<sup>5</sup>, Hendrik Heinz<sup>1,2\*</sup>

<sup>1</sup> Department of Chemical and Biological Engineering, University of Colorado at Boulder,  
Boulder, CO 80309, USA

<sup>2</sup> Materials Science and Engineering Program, University of Colorado at Boulder, Boulder, CO  
80309, USA

<sup>3</sup> Department of Physics, Michigan Technological University, Houghton, MI 49931, USA

<sup>4</sup> Department of Mechanical Engineering, Pennsylvania State University, University Park, PA  
16802, USA

<sup>5</sup> Department of Mechanical Engineering - Engineering Mechanics, Michigan Technological  
University, Houghton, MI 49931, USA

\* Corresponding author: [hendrik.heinz@colorado.edu](mailto:hendrik.heinz@colorado.edu)

## Abstract

The Interface force field (IFF) enables accurate simulations of bulk and interfacial properties of compounds and multiphase materials. However, the simulation of reactions and mechanical properties up to failure remains challenging and expensive. Here we introduce the Reactive Interface Force Field (IFF-R) to analyze bond breaking and failure of complex materials using molecular dynamics simulations. IFF-R uses a Morse potential instead of a harmonic potential as typically employed in molecular dynamics force fields to describe the bond energy, which can render any desired bond reactive by specification of the curve shape of the potential energy and the bond dissociation energy. This facile extension of IFF and other force fields that utilize a harmonic bond energy term allows the description of bond breaking without loss in functionality, accuracy, and speed. The method enables quantitative, on-the-fly computations of bond breaking and stress-strain curves up to failure in any material. We illustrate accurate predictions of mechanical behavior for a variety of material systems, including metals (iron), ceramics (carbon nanotubes), polymers (polyacrylonitrile and cellulose I $\beta$ ), and include sample parameters for common bonds based on using experimental and high-level (MP2) quantum mechanical reference data. Computed structures, surface energies, elastic moduli, and tensile strengths are in excellent agreement with available experimental data. Non-reactive properties are shown to be essentially identical to IFF values. Computations are approximately 50 times faster than using ReaxFF and require only a single set of parameters. Compatibility of IFF and IFF-R with biomolecular force fields allows the quantitative analysis of the mechanics of proteins, DNA, and other biological molecules.

## 1. Introduction

The prediction of deformation and failure properties of advanced functional materials from the atomistic scale to the microstructure and macrostructure is a grand challenge in materials science.<sup>1-</sup>

<sup>3</sup> The interplay of chemistry, cross-linking in polymers, hierarchical molecular-driven assembly, defects, and multi-scale dynamics facilitates a broad range of chemical, elastic, plastic, and failure properties. The difficulty is that experimental and computational methods for probing the stress response mechanisms from the molecular level to the continuum length scale are limited in experiments and in modeling. Molecular Dynamics (MD) simulations are widely used to complement gaps in experimental techniques, especially difficult-to-access physical and chemical processes in atomic-level resolution up to the large nanometer scale and within femtosecond to millisecond time scales.<sup>4-7</sup> MD allows for monitoring of molecular recognition, assembly, dynamics, and mechanical properties often in greater resolution than experiments.<sup>8-11</sup> In spite of limitations in size and time scales, understanding by MD simulations can increasingly guide the engineering of materials with enhanced properties, and predictions of the role of variable compositions, defects, chemical reactions, and processing conditions are feasible.

MD simulations use a force field to describe all possible atomic interactions and geometries through associated energy expressions and corresponding parameters.<sup>6</sup> These types of interactions can include harmonic bond stretching based on equilibrium bond lengths and bond vibrational constants, Coulomb interactions with atomic charges, and nonbonded Lennard-Jones potentials with equilibrium atomic distances and atomic cohesion energy. Currently, many MD force fields (IFF, PCFF, AMBER, CVFF, CHARMM, OPLS-AA) use harmonic bond energy terms which make them incapable of bond-breaking and bond-forming predictions, unless the bonded terms are replaced with nonbonded terms or more specific modifications are introduced. Specifically, the

Interface force field (IFF) unifies the simulation of inorganic and organic compounds in high accuracy using well-defined representations of chemical bonding and atomic charges that introduce chemical specificity, interpretability, and consistency unseen in other force fields.<sup>4</sup> Therefore, it is uniquely prepared to capture reactive processes using suitable modification. IFF was also developed to be transferable and compatible with existing harmonic force fields such as CHARMM, PCFF, OPLS-AA, AMBER, COMPASS, DREIDING, and others by using the same principal energy terms, including 12-6 and 9-6 options for the Lennard-Jones potential.<sup>4</sup> For example, the energy expression for a harmonic class II representation of IFF (same as PCFF) is:

$$\begin{aligned}
 E_{pot} = & \sum_{ij \text{ bonded}} \sum_{n=2}^4 K_{rn,ij} (r_{ij} - r_{0,ij})^n + \sum_{ijk \text{ bonded}} \sum_{n=2}^4 K_{\theta n,ijk} (\theta_{ijk} - \theta_{0,ijk})^n \\
 & + \sum_{ijkl \text{ bonded}} \sum_{n=1}^3 V_{\varphi n,ijkl} [1 - \cos(n\varphi_{ijkl} - \varphi_{0n,ijkl})] \\
 & + \sum_{ijkl \text{ bonded}} K_{\chi,ijkl} (\chi - \chi_{0,ijkl})^2 + E_{cross} \\
 & + \frac{1}{4\pi\epsilon_0\epsilon_r} \sum_{ij \text{ nonbonded}} \frac{q_i q_j}{r_{ij}} \\
 & + \sum_{ij \text{ nonbonded}} \epsilon_{0,ij} \left( 2 \left( \frac{r_{0,ij}}{r_{ij}} \right)^9 - 3 \left( \frac{r_{0,ij}}{r_{ij}} \right)^6 \right)
 \end{aligned} \tag{1}$$

In eq 1, we see that the total potential energy is a summation of potentials associated with bond stretching, angle bending, dihedral torsion, improper torsion, cross-interaction terms (not used in new additions), Coulomb interactions, and van der Waals interactions (9-6 Lennard-Jones potential). Hydrogen bonds are inherently represented by atomic charges and the LJ potential. The

variables  $r$ ,  $\theta$ ,  $\varphi$ , and  $\chi$  denote instantaneous bond length, bond angle, dihedral angle, and improper torsion angles, respectively, and the variables with the subscript zero represent the corresponding equilibrium values between atoms  $i, j, k, l$  (only the harmonic term with  $n = 2$  for bonds and angles is needed in IFF).<sup>12</sup> The variables  $K_r$ ,  $K_\theta$ , and  $K_\chi$  are bond, angle, and improper torsion bond constants, respectively.  $V_\varphi$  are dihedral constants,  $q_i$  are the atomic charges,  $r_0$  the equilibrium nonbond distance, and  $\epsilon_0$  is the Lennard-Jones well-depth.

Specifically, IFF is an all-atom force field created with the focus of reproducing the key physical, chemical, and surface properties of every compound included in the force field. IFF parameters were optimized such that lattice parameters usually deviate  $<0.5\%$  from experiment, surface and hydration energies  $<5\%$ , and mechanical properties typically (not always)  $<10\%$ .<sup>4</sup> The reliability of IFF models is higher than ReaxFF, which is limited in simulating interfaces, and in most instances higher than common density functionals that struggle with descriptions and interpretations of exchange-correlation energies.<sup>13-15</sup> The current list of compounds with IFF parameters includes layered silicates, silica, phosphates, sulfates, cement minerals, FCC metals, MoS<sub>2</sub>, graphitic materials, gas molecules, oxides, and several polymers. To enhance the property predictions of various graphitic structures and  $\pi$ -conjugated molecules, IFF incorporates virtual  $\pi$ -electrons on the corresponding carbon atoms,<sup>16</sup> which has been shown to improve binding energy predictions by nearly an order of magnitude relative to all known prior models.<sup>17</sup>

However, a major disadvantage of classical MD simulations, including IFF, is the difficulty to simulate bond dissociation and formation as would be observed in chemical reactions and mechanical failure of materials. The development of the Reactive Force Field (ReaxFF) by Adrian Duin and Bill Goddard aimed to address the limitations for bond dissociation in large-scale MD simulations through the use of a bond order potential, albeit at the cost of parameter

interpretability and difficult customizability.<sup>18</sup> While ReaxFF is able to predict bond breaking, the required energy correction terms greatly diminish computational efficiency. Also, ReaxFF parameters must be trained on individual molecular systems under specific conditions to make viable predictions. As a result, atomic behavior is heavily dependent on the parameter set used, leading to reliability concerns when calculating properties for systems and conditions not directly associated with the training systems. In contrast, IFF allows to mix and match validated compounds in multiphase systems without loss in accuracy and thrives on using chemical analogy to parameterize new compounds (which are then still required to undergo systematic validation).

This paper augments IFF and as another example, PCFF, to simulate bond breaking reactions in an efficient, accurate, and interpretable way, using a clean substitution of the harmonic bond energy expression for a Morse bond energy expression for a subset of atoms or for all atoms (Figure 1). We discuss the necessary theory and parameter changes, details of the underlying bond dissociation curves, and validation of the resulting reactive Interface force field (IFF-R). IFF-R is shown to yield insights into bond breaking, reproduce experimentally determined stress-strain curves and failure strengths, and maintain the same high level of performance for bulk and interfacial properties as is characteristic for IFF. We illustrate examples for the prediction of mechanical behavior of a range of material types, including single-wall carbon nanotubes (SWCNT), syndiotactic polyacrylonitrile (PAN) crystal, cellulose I $\beta$  crystal, and  $\gamma$ -iron. The computational speed is 50x higher than ReaxFF. We also discuss limitations and follow-on directions.

## **2. Results and Discussion**

**2.1. Description of the Approach.** The aim of IFF-R consists in identifying chemical bonds that are susceptible to break and to replace the 2-parameter harmonic potential with a 3-parameter Morse potential for these bonds (Figure 1a, b). The protocol begins with a survey of bond dissociation energies using experimental reference data in readily available compendia, reviews, and databases (Figure 1c).<sup>19-22</sup> It is helpful to identify weaker bonds in a molecular structure or polymer that are more likely to dissociate under large mechanical loads. Typically, these bonds are more important to be represented by a Morse potential, which then should precisely capture the bond dissociation curve and bond energy to allow failure (Figure 1a). All other remaining bond types can still use the harmonic potential.

The process of incorporating these bond breaking capabilities is quite simple for bonds that have already been parameterized and validated using the harmonic bond energy expression (see tutorial in the Supporting Files). The protocol then proceeds with plotting the bond energy vs atomic distance using the harmonic bond potential for a specific pair of atoms  $ij$  (Figure 1a, b). Next, using experimental values<sup>19-22</sup> or quantum mechanical data<sup>23</sup> for the bond dissociation energy  $D_{ij}$ , we plot the Morse potential curve using the Morse bond energy equation for the same pair of atoms (Figure 1b). Thereby, the equilibrium bond length  $r_{o,ij}$  remains the same in both potentials, and the parameter  $\alpha_{ij}$  can be tuned such that the shape of the Morse energy curve matches that of the harmonic energy curve near the resting state (lowest energy) (Figure 1a). Hereby, the shape of the harmonic energy equation is determined by two variables that describe the bond characteristics between atoms  $i$  and  $j$ : the equilibrium bond distance  $r_{o,ij}$  and the bond stiffness coefficient  $K_{r,ij}$ . The Morse potential uses the same equilibrium bond distance  $r_{o,ij}$ , and the  $\alpha_{ij}$  values for many chemical bonds are  $2.1 \pm 0.2 \text{ \AA}^{-1}$  (Figure 1d), which makes an initial estimate of the Morse energy curve easy once the dissociation energy  $D_{ij}$  is known.<sup>24</sup> Therefore, when using

the Morse bond energy equation, three variables describe the bond behavior: (1) the equilibrium bond distance ( $r_{o,ij}$ ); which is the same as in the harmonic potential, (2) the width of the bond potential well ( $\alpha_{ij}$ ); which is close to  $2.1 \text{ \AA}^{-1}$  and can be fitted to match the harmonic curve characterized by  $K_{r,ij}$  near equilibrium ( $\alpha_{ij}$  is inversely proportional to width), and (3) the bond dissociation energy ( $D_{ij}$ ), which can be obtained from experimental data for thousands of bonds<sup>19-22</sup> or from quantum mechanical calculations.<sup>23</sup> The width of the bond potential  $\alpha_{ij}$  as well as  $K_{r,ij}$ , respectively, can also be adjusted by matching the wavenumber of bond vibrations obtained in MD simulations to experimental data from Infrared and Raman spectroscopy, as is performed in the validation of IFF.<sup>25</sup>

The method for parameterizing Morse bonds was applied to seven bond types in this study (Figure 1d). The remaining parameters, i.e., non-reactive bonds, all angles, torsions, improper torsions (out-of-plane), charges, and LJ parameters, were retained from IFF or PCFF.<sup>26</sup> The simplicity of the method enables users of non-reactive force fields such as PCFF, CVFF, CHARMM, OPLS-AA, AMBER, COMPASS, to quickly and easily develop Morse parameters for any given bonded pair. Also, the clean replacement of harmonic bonds by Morse bonds offers an accurate and interpretable description of mechanical bond dissociation without the need for complex fit parameters in a manner that has yet to be realized in reactive force fields.<sup>18, 27, 28</sup>

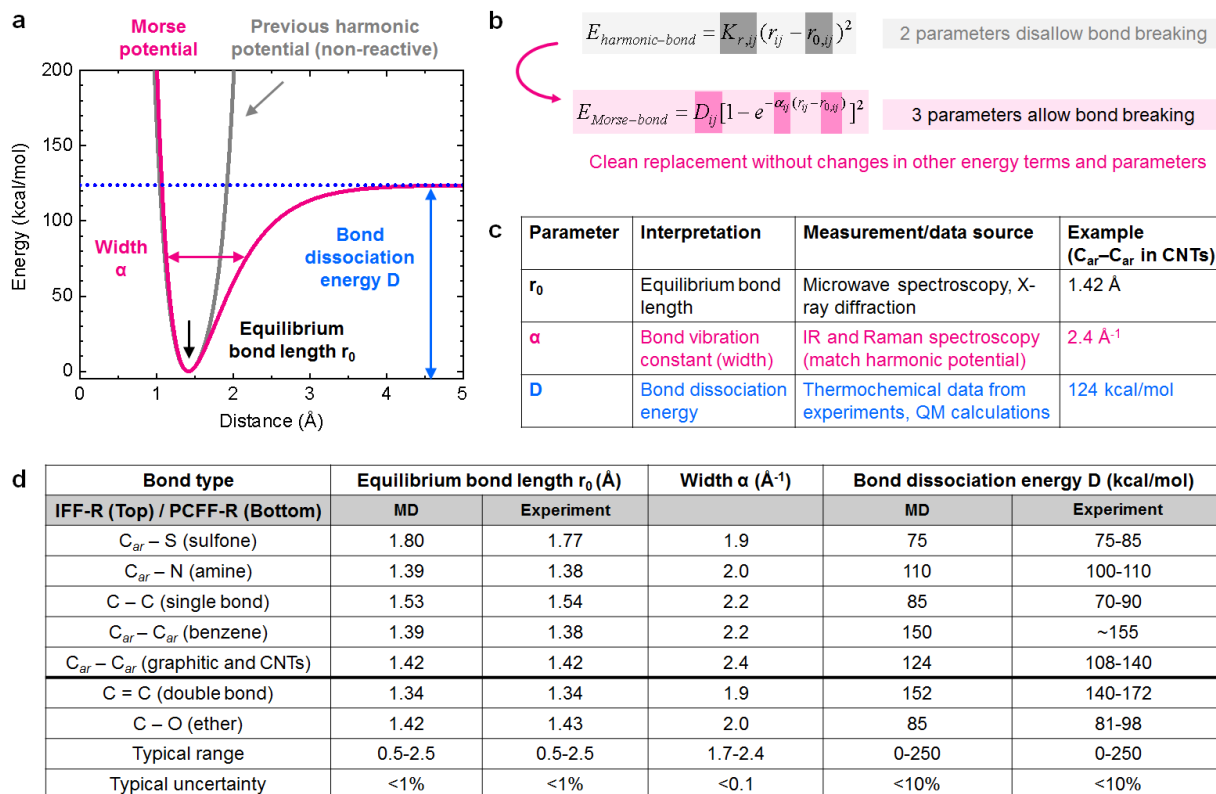


**Figure 1.** Concept of IFF-R. Substitution of non-reactive harmonic bond potentials in IFF for reactive Morse bond potentials leads to IFF-R, and similar modification of other harmonic force fields is feasible. (a) Bond energy vs. bond distance using the Morse potential in the MMMff (pink) and the equivalent harmonic bond potential in the harmonic force field (gray) for the example of a graphitic  $C_{ar}-C_{ar}$  bond. The Morse potential is tuned to fit the harmonic bond potential near equilibrium without changes in other parameters. (b) Equations and parameters in the harmonic bond potential and in the Morse bond energy. All three parameters in the Morse potential  $r_{0,ij}$ ,  $\alpha_{ij}$ , and  $D_{ij}$  can be obtained from experimental data. If  $r_{0,ij}$  and  $K_{r,ij}$  are known from IFF or another parent force field, only  $D_{ij}$  needs to be determined using additional information from experimental databases (refs. <sup>19-22</sup>) or high-level quantum mechanical calculations. (c) Interpretation, sources, and examples of Morse bond parameters. Since the parameters correspond to experimental data, MMM involves no adjustable parameters, or only in a small range. (d) Table of Morse parameters

for selected bonds in IFF-R (above bold line) and PCFF-R (below bold line). New chemical bonds can be added and customized. Experimental data for  $r_{0,ij}$  are from ref. <sup>19</sup>. Experimental data for  $D_{ij}$  are from refs. <sup>19-22</sup>. Data for all carbon-carbon bonds additionally consider ref. <sup>29</sup>, and the data for carbon-carbon bonds in graphite and carbon nanotubes also consider ref. <sup>30</sup> (DFT-based). The range of bond energies from refs. <sup>19-22, 29</sup> can be significantly narrowed down once the specific chemical environment of the bonds is specified (<3% uncertainty).

**2.2. IFF-R Morse Parameterization and Customizability.** We considered a set of small organic monomers used in composites to examine details of bond dissociation (Figure 2). Bond dissociation simulations were performed on diethyltoluenediamine (DETDA) (Figure 2a, b) and 4,4'-diaminodiphenylsulfone (4,4'-DDS), which are used to prepare polyurethanes, polyimides, epoxy resins, and CNT/epoxy composites (Figure 2c-f).<sup>31-33</sup> The data for each type of bond shows differences between quantum methods whereby MP2 can be considered more accurate than DFT with B3LYP. In the bond energy profiles calculated with MP2 and DFT, the energies may diverge toward negative infinity at bond distances larger than 2.5 Å, hence the data is only shown for shorter distances (Figure 2). IFF-R and ReaxFF (ref. <sup>34</sup>) simulations can be carried out for larger bond lengths (>2.5 Å). Data by ReaxFF looks similar to quantum mechanical results, although somewhat more irregular, and IFF-R curves were smoothly adjusted to approximate MP2 or DFT values (Figure 2a-f). We also note some differences relative to average C(ar)-C(ar), C-N, and C-S bond dissociation energies from the literature (Figure 1d).<sup>19-22, 29</sup> These changes are related to substituent effects.

Specifically, in the amino-substituted DETDA, a ~10 kcal/mol lower bond energy of the 2,3 bonds (MP2 in Figure 2a) versus the 1,2 and 3,4 bonds (MP2 in Figure 2b) is seen. The

difference is related to more double bond character of the 3, 4 bonds and 1, 2 bonds compared to the 2, 3 bonds, consistent with an analysis of the resonance structures of DETDA (see Figure S1 in the Supporting Information). An even larger difference is seen for the bonds in 4,4'-DDS, which experience a push-pull effect by the NH<sub>2</sub> and SO<sub>2</sub> groups in the 1, 4 positions (MP2 in Figure 2c, d). The 2,3 carbon-carbon bonds in 4,4'-DDS have almost full double bond character and are ~30 kcal/mol stronger than the 1,2 and 3,4 bonds (Figure 1d), related to an electron distribution consistent with NH<sub>2</sub>(+)=C1(C5)-C2(H)=C3(H)-C4=SO<sub>2</sub>(C4')(-).<sup>35</sup> These effects can be considered in IFF-R as needed through the assignment of specific atom types (not shown here for simplicity). Substituent effects are less accessible and harder to modify in other reactive simulations such as with ReaxFF, which would require more complex reparameterizations (ReaxFF in Figure 2c, d). The MP2 bond scans and IFF-R representation also indicate different bond strengths for C<sub>ar</sub>-S and C<sub>ar</sub>-N bonds, e.g., which are only on the order of 75-85 kcal/mol for C<sub>ar</sub>-S (Figure 2e) and 110 kcal/mol for C<sub>ar</sub>-N (Figure 2f) in comparison to 120-170 for typical C(ar)-C(ar) bonds (Figure 2a-d).

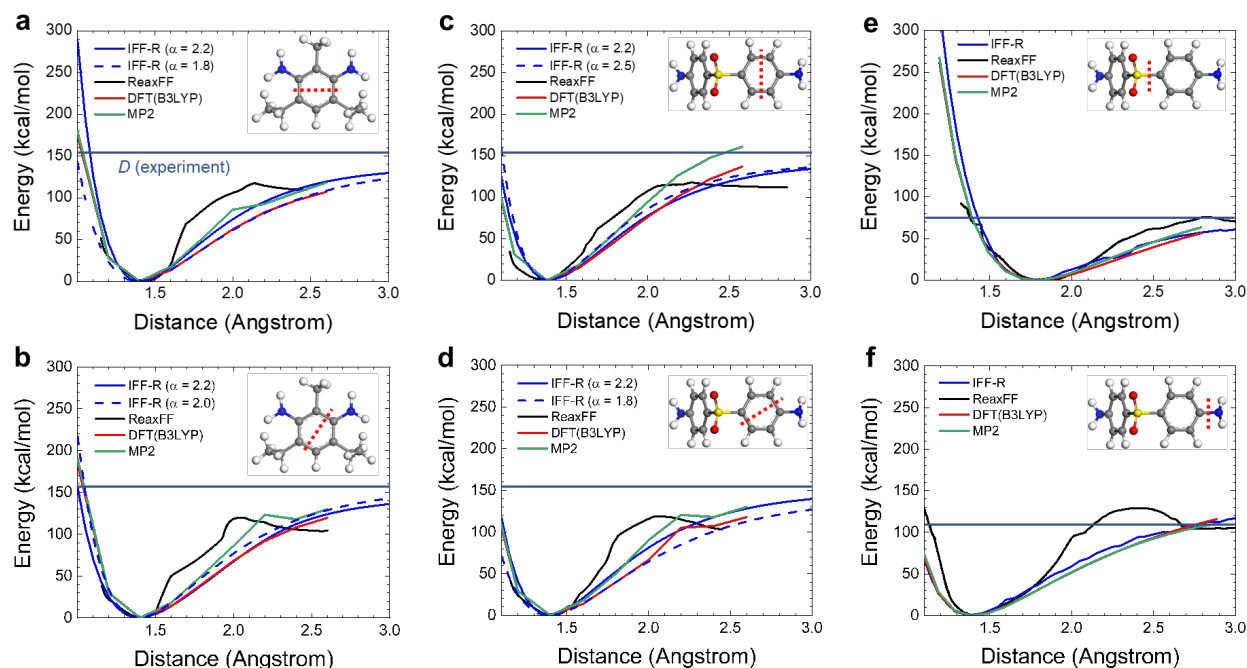


**Figure 2.** Examples of bond scans. The dissociation of several bonds in two amine monomers (DETDA and 4,4'-DDS) was simulated using MP2, DFT (B3LYP), ReaxFF (ref. <sup>34</sup>), and with the chosen IFF-R parameters. The red dashed lines represent the bonds that dissociated in each simulation. The horizontal blue line represents estimates of bond dissociation energies based on experimental studies (similar chemistry without exact substitution pattern, refs. <sup>19-22, 29</sup>). The blue dashed curves demonstrate IFF-R customizability and represent alternative quantum method parameterization. (a, b) Dissociation curves of aromatic carbon-carbon bonds in DETDA in two different molecular planes. Bonds in plane (b) feature slightly higher double bond character and higher energy than in plane (a). (c, d) Dissociation of aromatic carbon-carbon bonds in 4,4'-DDS in two different planes. The 2, 3 bonds in (c) are stronger than the 1, 2 and 3,4 bonds in (d) due to push-pull effects from the polar substituents ( $\text{NH}_2(+)=\text{C1}-\text{C2}=\text{C3}-\text{C4}=\text{SO}_2(-)$ ). Details are most clearly seen at the MP2 level (not specifically included in IFF-R here for simplicity). (e, f) Dissociation curve of the carbon-sulfur bond and carbon-nitrogen bonds in 4,4'-DDS.

In summary, IFF-R incorporates bond dissociation energies on the basis of verified experimental literature and high-level (e.g. MP2) quantum mechanical data (Figure 2a-f). Since all three parameters ( $r_0$ ,  $\alpha$ , and  $D$ ) can be conveniently obtained in good accuracy using extensive databases based experimental measurements,<sup>19-22, 29</sup> IFF-R offers an interpretable set of parameters. The parameters can be further customized for any known pair of bonded atoms with the assistance of high-level quantum mechanical calculations to tune the  $\alpha$  and  $D$  parameters so that the bond dissociation curve computed with IFF-R matches the quantum mechanical reference (see dashed IFF-R lines with different  $\alpha$  values in Figure 2a-d). In this manner, specific details of electronic structure can be captured which is not easily afforded by other reactive molecular dynamics force fields. The analysis of specific chemical environments (substituents, nearby reactions) is recommended and can be incorporated in IFF-R as needed. It is also helpful to be aware of differences between “bond dissociation energies” that apply to a particular bond and are most suitable for IFF-R versus “average bond energies”, which are an average over the bond dissociation energies of all equivalent bonds in a molecule and usually differ from the energy required to break the first such bond.

**2.3. Applications of IFF-R and Similar Force Fields: Simulations of Stress-Strain Curves and Failure.** Simulations of stress-strain curves are critical to determine how a material will perform when subjected to external forces. Here we focus on the Young’s modulus and uniaxial tensile strength, which are widely used to characterize a material’s mechanical performance. Hereby, Young’s modulus characterizes the material’s initial linear stress-strain response and the tensile strength is the stress at which the material critically fails (right hand side of Figure 3). Atomic-level deformations and the occurrence of bond scission upon failure can be

clearly seen, and a significant gain in computational speed relative to ReaxFF, which leads to similar results. More quantitatively, the stress-strain curves were compared to available experimental data or high-level quantum mechanical results (Figure 4). The agreement with the reference data is within 10% deviation for most mechanical property predictions, and often better than ReaxFF (Table 1). The ability of MMMff's to predict and show realistic material failure for 4 different classes of materials including ceramics (CNTs) (Figure 3a), polymers (PAN) (Figure 3b), biopolymer (cellulose) (Figure 3c), and metals (iron) (Figure 3d) illustrates the viability to simulate bond breaking under large mechanical deformations. Furthermore, additional Morse bond parameterization for IFF-R is demonstrated through matching of Young's Modulus and ultimate tensile strength calculations (when available) to experimental refs.<sup>36</sup> or quantum calculations for the SWCNT (Figure 3a) and PAN crystal (Figure 3b) respectively.

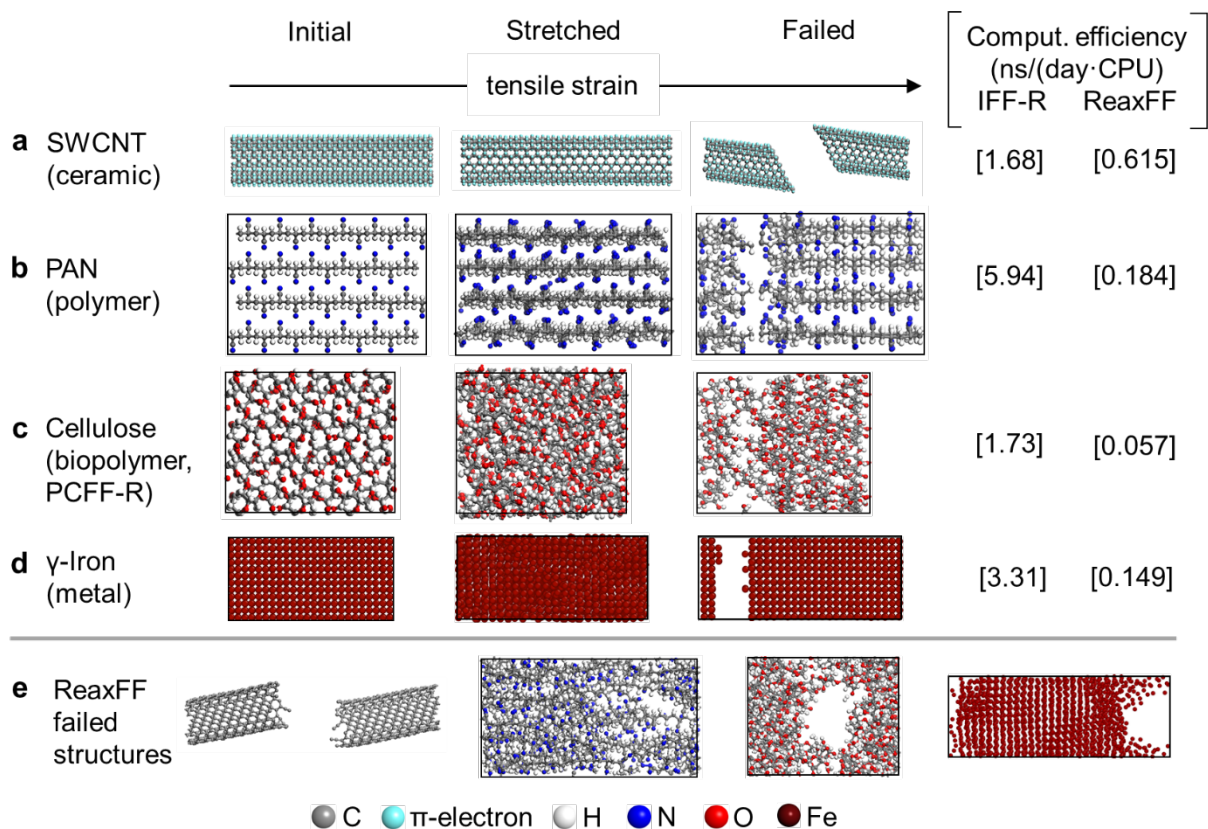


**Figure 3.** Responses of different materials to applied stress during MD simulation with IFF-R (PCFF-R in case of cellulose). Snapshots are shown at the initial timestep, near the middle of the tensile simulation, and at failure. (a) A single-walled carbon nanotube (SWCNT) with a diameter of 1 nm, (b) a syndiotactic poly(acrylonitrile) (PAN) crystal, (c) a cellulose I $\beta$  crystal (ref. <sup>37</sup>), and (d) a crystal of  $\gamma$ -iron. (e) Snapshots at failure with ReaxFF (refs. <sup>38-40</sup>) for the same systems. The average computational efficiency is indicated on the right-hand side in nanoseconds per day and CPU core, assuming 1 fs time steps. Accordingly, MMMff simulations can be up to 50x's faster than ReaxFF when using a timestep as low as 0.5 fs. It is also possible to increase the time step in IFF-R to 2 fs and higher, including constraints on H atoms and  $\pi$  electrons, if present, which enables further increases up to 100x relative to ReaxFF.

The replacement of harmonic potentials with Morse bond-stretching potentials in IFF-R and other modified force fields is thus a suitable approach for modeling bond scission. The carbon nanotube and  $\gamma$ -iron show relatively smooth cleavage planes (Figure 3a, d and Figure 4a, b, e). The mechanical failure of the polymers is shown to initiate from breaking of load-bearing bonds in single polymer chains (Figure 3b, c). However, at the moment of bond scission, the atoms of the broken polymer bonds absorbed the released energy in the form of kinetic energy with high velocities that hamper the effective integration of the equations of motion in LAMMPS for the time steps utilized. This caused the simulations to cease for bulk polymeric materials before all polymer chains would be dissociated, corresponding to failure of the entire bulk polymer model. These shortcomings could be addressed by selecting a time step of 0.1 fs and limiting atomic movement. Such modifications are not needed to compute the tensile modulus and only recommended to analyze the tensile strength. There is some uncertainty when computing the failure mechanism until scission of all possible bonds, past reaching the tensile strength in this manner, since the material behavior after failure is not fully described. Despite this, the ultimate strength can be determined (Figure 4b,c), and a more comprehensive computational method to address the issue of bulk polymeric failure is under investigation.

The results show that the parameters developed for IFF-R and PCFF-R can be utilized for simulating accurate stress-strain curves for a broad range of material systems without the need for highly specialized parameter training (Figure 4).

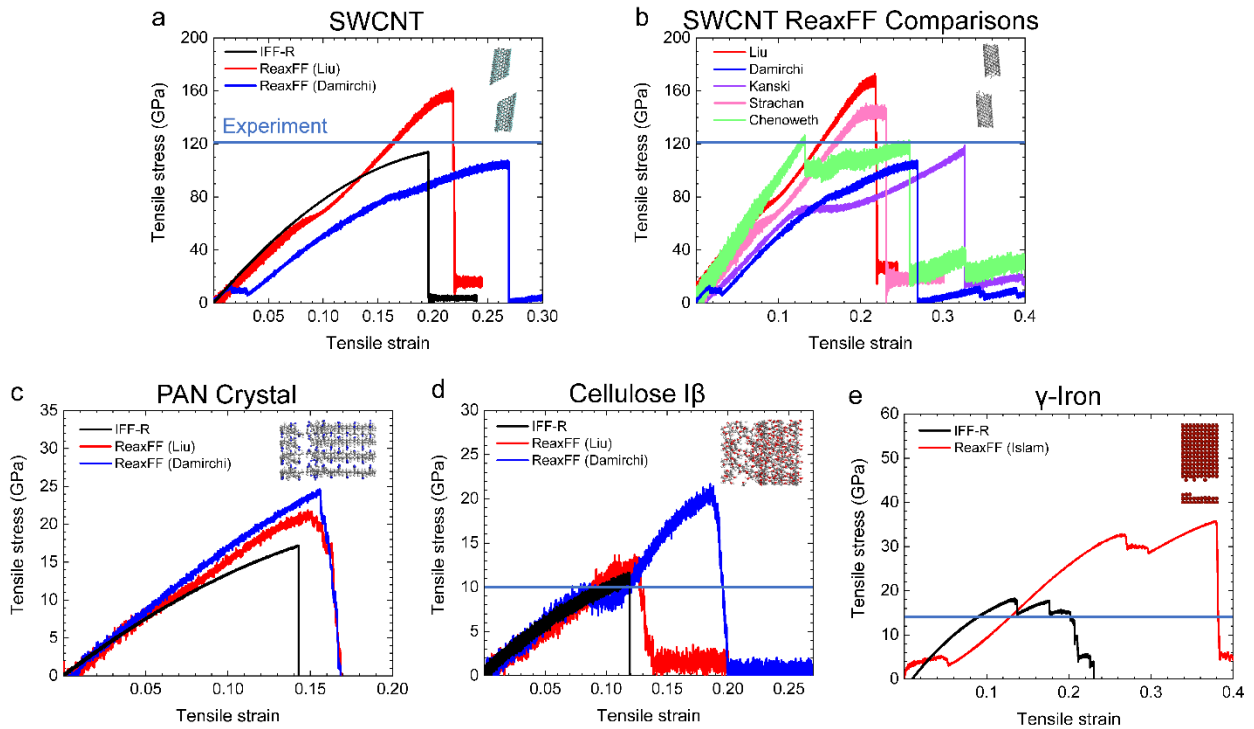


**Figure 4** Stress-strain curves under uniaxial tensile strain using IFF-R, PCFF-R, and ReaxFF parameter sets. When available, the experimentally determined tensile strengths (or high-level theory estimates) are shown as horizontal lines. (a, b) SWCNT of 1 nm diameter and comparison to simulations with ReaxFF (refs. <sup>38, 39, 41-43</sup>). IFF-R yields one well-defined result whereas ReaxFF offers at least 5 different parameter sets that have more than 50% variation in strength, ductility, and curve shape (b). (c) Syndiotactic, crystalline polyacrylonitrile (PAN). (d) Crystalline I $\beta$  cellulose. (e)  $\gamma$ -iron. The material at failure using MMMff's (and ref. <sup>38</sup> in (b)) are shown in the top right corner of each of the stress-strain plots. MMMff's perform very well in comparison to experiment and shows lower ambiguity and deviation relative to ReaxFF, which is particularly important for composite materials.

The IFF-R parameters for SWCNTs were tuned by incrementally increasing the  $\alpha$  Morse bond parameter until the predicted failure strength and Young's Modulus of the SWCNTs closely

matched that of experimental and theoretical studies (Figure 4a).<sup>36, 44-46</sup> The Damirchi parameters (ref. <sup>39</sup>) predict that there should be some initial CNT yielding around 0.01 strain. This is not usual for SWCNT with a diameter of 1 nm and could be due to the Damirchi parameters being optimized for flattened CNTs.<sup>39</sup> It is also shown that material response can vary widely depending on the ReaxFF parameter set used (Figure 4b). The abundance of available ReaxFF parameters makes it difficult to determine which set of parameters, if any, will produce the most reliable property predictions for a given material. In addition, a ReaxFF uses only one atom type for each element and the user is required to specify only one parameter set for carbon atoms, for example, which would lead to discrepancies in a composite material with multiple components (e.g. containing CNT, PAN, and cellulose) (Figure 4c, d). IFF-R overcomes this limitation as every compound or groups thereof are separately and flexibly parameterized.

For 100% crystalline PAN (Figure 4c), we have no certain reference data for the failure strength, however, elastic constants could be estimated using the Cambridge Serial Total Energy Package (CASTEP) program (Table 1).<sup>47</sup> IFF-R parameters for the C-C single bond did not need to be tuned from the general MMM, such that the mechanical property predictions match that of the CASTEP reference. It is shown that the Young's Modulus of PAN using IFF-R is within 10% deviation to that of the CASTEP predictions (Table 1). Both the Liu and Damirchi ReaxFF parameters demonstrate similar PAN mechanical behavior but have greater deviation from the CASTEP predictions. All methods used show a brittle fracture of the PAN crystal which is expected.

For crystalline I $\beta$  cellulose (Figure 4d), the PCFF-R and Liu parameters (ref. <sup>38</sup>) have strengths in the range of the experimental values while the Damirchi parameter set predicts a significantly higher strength. The Damirchi parameters also demonstrate some yielding around

0.08 strain, which one would not expect from a 100% crystalline polymer material. This could be because the Damirchi parameters could not be used with the low-gradient correction for long-range London Dispersion forces developed by Liu et al., which may influence the effect of hydrogen bonding in cellulose, and ultimately cellulose's mechanical performance.<sup>38, 39</sup>

For the  $\gamma$ -iron crystal, which was modeled after the primary lattice structure of austenitic stainless steel (Figure 4d), the IFF-R parameters provide predictions for the failure strength close to experimental values, and demonstrate the characteristic yielding of metals.<sup>9</sup> The Islam ReaxFF parameter set (ref. <sup>48</sup>) has a much higher, unrealistic failure strength and yield behavior. The poor strength prediction by ReaxFF parameters could be related to lack of specialized training for the tensile simulation of  $\gamma$ -iron, however, it is difficult for a user to find documentation and the many parameters have no clear physical interpretation.

**Table 1.** Comparison of Young’s Modulus and the tensile strength for different materials classes using experimental measurements, molecular dynamics simulation with IFF-R, MMMff’s and ReaxFF. The systems include a SWCNT of 1 nm diameter (ceramic), crystalline syndiotactic PAN, and crystalline I $\beta$  cellulose (polymers), and  $\gamma$ -iron (metal).

	SWCNT		PAN		Cellulose (PCFF-R)		$\gamma$ -Iron (111)	
	Modulus (GPa)	Strength (GPa)	Modulus (GPa)	Strength (GPa)	Modulus (GPa)	Strength (GPa)	Modulus (GPa)	Strength (GPa)
Experiment	1007 $\pm$ 118 <sup>a</sup>	121.6 $\pm$ 22 <sup>a</sup>	172 (DFT)	N/A	150 $\pm$ 5.0 <sup>49</sup>	4-10 <sup>50</sup>	210 $\pm$ 10 <sup>51</sup>	13.1 $\pm$ 1.5 <sup>52</sup>
IFF-R (PCFF-R)	1001 $\pm$ 3.0	115 $\pm$ 1.5	179 $\pm$ 8.0	17 $\pm$ 2.0	118.9 $\pm$ 4.0	11.6 $\pm$ 1.25	137 $\pm$ 2.3	17 $\pm$ 0.8
ReaxFF <sup>b</sup>	752 $\pm$ 2.0	173 $\pm$ 2.0	198 $\pm$ 6.0	22 $\pm$ 2.0	121.4 $\pm$ 3.9	12.9 $\pm$ 2.0	4627 $\pm$ 5.0	35 $\pm$ 5.0

<sup>a</sup> From tensile testing of a 2.1 nm CNT using a micro/nanoscale material testing system.<sup>36</sup>

<sup>b</sup> Using parameters set from Liu et al.<sup>38</sup> Values may change for a different parameter set.

Experimental results for  $\gamma$ -iron are similar to the mechanical properties of steel.

For many of the simulated materials, the IFF-R parameters predict strengths within the standard error of the experimentally determined values (Table 1). However, the predicted modulus values for  $\gamma$ -iron and cellulose using the PCFF-R parameters deviated greater than 20% from what is experimentally determined. These deviations are a result of opportunities to improve the parameters (especially cellulose in PCFF), as well as inherent limitation of models (Table 1). The

optimization of non-bonded parameters for cellulose and new models with virtual electrons for iron are beyond the scope of this work and not critical to demonstrate the value of IFF-R to simulate bond dissociation and broad applicability. Also, it has been shown that 12-6 Lennard-Jones (LJ) models (CVFF, AMBER, CHARMM, OPS-AA, DREIDING) on average demonstrate improved Young's Modulus predictions over the 9-6 LJ equivalents for metals.<sup>9</sup> We recommend using IFF/IFF-R 12-6 LJ models when tensile properties of metals are desired. In this case, also no definition of Morse bonds is required due to simplicity of the LJ potential.

**2.4. Compatibility and Transferability.** For the function of IFF-R and similar force fields with reactive extensions, it is important to retain and validate the modularity of bond potentials. We find that the replacement of the harmonic bond potentials in IFF with the Morse bond potentials in IFF-R, as described earlier, enables bond dissociation without losing the accuracy of the key physical, chemical, and interfacial property predictions in IFF (Table 2) for propionitrile (similar parameters as PAN) and graphite (similar parameters as CNT). Accordingly, the density and lattice parameters, as well as the vaporization energy of propionitrile and of glucose (using PCFF-R), and the surface energy of graphite using IFF-R remain the same as in IFF (or PCFF-R) within the statistical errors from the simulation (at least 2 ns). The density and the lattice parameters represent a quality check for reproducing the structures correctly. The surface or vaporization energies, respectively, represent a quality check on the energies, altogether validating the function of a Hamiltonian to accurately predict structures and energies. The lattice parameters are comparable between IFF and IFF-R, but not always matching the experimental references (Table 2). Hereby, the parameters for glucose were used as provided in PCFF with some improvements, and do not apply IFF standards for validation.

Accordingly, IFF and IFF-R predict a few percent higher propionitrile density, yet essentially the same values. Both force fields also show propionitrile vaporization energies within the range of experimental error and numerically very close values. For the glucose crystal, the lattice parameters provide a trend toward shrinking  $a$  and  $b$  parameters, and an expanding  $c$  parameter for PCFF and PCFF-R. Both force fields predict glucose crystal densities comparable to experiment, and again the same values. The vaporization energies (sublimation energies) are in reasonably good agreement. However, to thoroughly reproduce experimental data and IFF/IFF-R standards, PCFF parameters for glucose would need a major overhaul. For example, charges need to be reassigned along with more interpretable bonded and nonbonded parameters, potentially including stereoelectronic effects at the C1 carbon atoms. At this stage, new charge assignments were used (see Supporting Information) to avoid drastic differences in computed vaporization energy from the experimental reference. The predicted lattice parameters of graphite using IFF and IFF-R match experimental reference values, and the surface energy calculations for this material are nearly equivalent, as a result full validation in IFF format.

**Table 2.** Comparison of lattice parameters and surface (or vaporization) energies from experimental references and computational results using IFF and IFF-R. Equilibrium densities are given for liquid propionitrile, crystalline glucose, and bulk graphite. The lattice parameters for the glucose crystal and bulk graphite material are listed. The vaporization energy for propionitrile was

calculated with IFF/IFF-R parameters, while for glucose PCFF/PCFF-R parameters were utilized given. The surface energy of graphite was calculated using IFF and IFF-R.

Material		Lattice parameters (nm)		Density (g/cm <sup>3</sup> )	Vaporization energy (V) (kJ/mol) or surface energy (S) (mJ/m <sup>2</sup> )
		a, b, c	$\alpha, \beta, \gamma$		
Propionitrile	Expt	N/A		0.683	36.1 ± 1.6 (V)
	IFF	N/A		0.72	38.0 ± 2.0
	IFF-R	N/A		0.725	37.6 ± 2.5
Graphite	Expt	0.246, 0.426, 0.680	90°, 90°, 90°	2.26	186 ± 2.0 (S)
	IFF	0.247, 0.428, 0.675	89°, 90°, 90°	2.24	186 ± 5.0
	IFF-R	0.247, 0.428, 0.676	88°, 93°, 90°	2.23	188 ± 2.4
$\alpha$ -D-glucose	Expt	1.036, 1.483, 0.493	90°, 90°, 90°	1.56	181 ± 5.0 (V)
	PCFF	0.912, 1.268, 0.670	90°, 90°, 90°	1.54	178 ± 6.0
	PCFF-R	0.912, 1.267, 0.670	90°, 90°, 90°	1.55	178 ± 8.0

Another helpful comparison concerns the performance of IFF-R versus ReaxFF (Table 3). Hereby, energy differences are compared in the form of surface energies and vaporization energies, which are the basis for most thermodynamic properties as well as for mechanical properties, which

consist of derivatives of energy differences as a function of coordinate. The IFF-R parameters reproduce the surface energies and vaporization energies for the four materials with less than 5% deviation. For the graphitic materials modeled with virtual  $\pi$ -electrons, results for the surface energy were obtained within the standard deviation of the experimental reference values.<sup>53-55</sup> The deviations using ReaxFF are typically much higher, up to more than a factor ten. Hereby, the ReaxFF graphite structure was simulated using Liu et al ReaxFF parameters which do not include virtual  $\pi$ -electrons.<sup>38</sup> For the (111)  $\gamma$ -iron surface both the IFF-R and ReaxFF parameters reproduce experimental surface energy values with less than 2% deviation.<sup>56-58</sup> However, we note here that the ReaxFF parameters used for this simulation were different from those used in the tensile simulation (Figure 4e and Table 1). The Aryanpour ReaxFF parameters would deviate greater than 200% from the experimental reference, and therefore the Shin et al ReaxFF parameters were utilized here to calculate the surface energy of iron.<sup>59</sup> These differences also demonstrate that when the same ReaxFF parameter set is used for iron, some large deviation (order of 100%) in either surface properties or mechanical properties is inevitable, which is not the case with IFF and IFF-R. Both Liu and Damirichi ReaxFF parameter sets were used for the enthalpy calculations of propionitrile and glucose, however, only the Liu parameters are shown. Since only the Liu parameters could be calculated with the low-gradient van-der-Waals correction, they were determined to be a better comparison for non-bonded properties. The Damirichi results for the non-bonded property predictions can be found in the supporting information. The IFF-R parameter set reproduces experimental data for the vaporization energy of propionitrile and the modified PCFF-R parameters roughly the enthalpy of sublimation of glucose with uncertainties <5%.<sup>38, 60-63</sup> The parameters for propionitrile were modified to meet IFF and IFF-R standards.

**Table 3.** Comparison surface energies and vaporization energies for the 4 types of compounds, respectively, computed by IFF-R and ReaxFF relative to experimental reference values. The computed surface energies of high-melting solids (iron and graphite), vaporization energies of liquids (propionitrile) and sublimation energies of molecular solids (glucose) characterize the ability to predict interfacial properties.

Material	Experiment	IFF-R	Deviation (%)	ReaxFF	Deviation (%)
<b>Surface energy (mJ/m<sup>2</sup>)</b>					
Graphite	186 ± 2.0	188 ± 2.4	1.1	242 ± 2.5	30.1
γ-Iron (111)	2410 ± 12.0	2430 ± 7.0	0.8	2376 ± 8.0 <sup>a</sup>	1.4
<b>Vaporization energy of monomer (kJ/mol)</b>					
Propionitrile (PAN repeat unit)	36.1 ± 1.6	37.6 ± 2.5	4.4	49 ± 4.0	36
Glucose (Cellulose monomer)	181.7 ± 5.0	178 ± 8.0	1.7	173 ± 10	4.4

<sup>a</sup> The Shin et al ReaxFF parameters were used to calculate the surface energy of iron.<sup>59</sup> The Aryanpour et al ReaxFF parameter set would incur 200% deviation, leaving quite different choices to the user.

**2.5. Advances in Use of Morse Potentials.** Morse potentials have been offered in earlier force fields such as in CVFF.<sup>64</sup> However, then the functionality has not been widely used due to lack of accuracy and transferability. IFF-R increases the accuracy of key surface, interface, and mechanical properties by 10 to 100 times, which combined with the availability of orders of

magnitude higher computing power today, enables the use of Morse potentials to solve new problems in materials and biopolymer interfaces such as bond breaking and computation of reliable stress-strain curves in complex systems. We also demonstrate the compatibility and integration of Morse potentials into existing parameters for inorganic and organic compounds. Clean replacements are possible, and it is an advantage that not all bonds require a Morse potential as previously assumed. Therefore, existing harmonic bond energy and new Morse bond energy functions can be used side-by-side, enabling transferability, customization, and accurate integration of major aspects of the electronic structure. Hereby, IFF-R can rely on generic bond energies for rapid tests, however, IFF-R can incorporate specific bond energies from high-level QM calculations that accurately account for local conjugation, stereo-electronic, and substituent effects with relatively little effort and full interpretability. Such opportunities are not available by other reactive MD protocols (e.g. ReaxFF), which involve highly empirical and complex energy expressions and take up to ~50 times more simulation time.

### **3. Conclusion**

We introduce an effective method to replace nonreactive harmonic bond potentials with reactive Morse bond potentials in the Interface force field and in other typical harmonic force fields that then allow the simulation of bond breaking. We illustrate that this modification is rather easy to implement, does not require adjustments of other force field parameters when done correctly, that this method can be used to predict accurate stress-strain curves, tensile strengths, and moduli for different classes of materials. The similarity between IFF and IFF-R surface energy and enthalpy calculations verifies that this method retains accurate physical, chemical, and interfacial property predictions of the IFF parameters without the need for further parameter adjustments. The bond

parameters can be further enhanced by using results of local high-level quantum mechanical methods, such as precise bond dissociation curves, in a parameter-passing approach. This approach enables the creation of a reactive all-atom IFF-R force field with interpretable parameters, maintaining the same standards as IFF and validation by available experimental data. IFF-R is shown to be a convenient, computationally more efficient alternative to existing state-of-the-art reactive force fields such as ReaxFF. With the IFF-R parameter set, dependable and accurate large deformation material predictions can be made for organic and inorganic compounds, often more reliable than ReaxFF and directly applicable to complex multi-phase materials using one singular parameter set. The approach for introducing bond dissociation provides a foundation to extend this concept to a limitless number of bonded pairs. The efficiency and interpretability of IFF-R can also be utilized to create rather realistic data sets for machine learning platforms.

#### **4. Computational Methods**

The following simulation setup applies to all simulations unless otherwise stated. All material structures were built using Materials Studio v7.0.<sup>65</sup> The molecular dynamics simulations were performed using the Large-scale Atomic/Molecular Massively Parallel Simulator (LAMMPS). At the outset, the systems were subjected to energy minimization for up to 10,000 steps with an energy tolerance of  $10^{-4}$  and a force tolerance of  $10^{-6}$  kcal/(molÅ). Subsequent molecular dynamics simulations with IFF or IFF-R used the PPPM K-space solver with a relative energy tolerance of  $10^{-4}$  for Coulomb interactions and a short-range cutoff at 8.0 Å. The summation of Lennard-Jones interactions (van der Waals interactions) was carried out with a spherical cutoff at 12.0 Å. The materials were simulated at a temperature of 298.15 K using the Nose-Hoover thermostat and barostat, and temperature dampening within 100.0 timesteps in the NPT ensemble or NVT

ensemble. The NPT ensemble was used for equilibration of crystal structures and to obtain enthalpy values for bulk materials. The NVT ensemble was used for the tensile simulations and to obtain the enthalpies for materials in the vapor phase. Initial atomic velocities were set using a Gaussian distribution.

**4.1. Bond Scans.** The bond dissociation simulations using molecular dynamics were performed by building multiple atomic structures in Materials Studio v7.0 in which the specified bond between atoms *i* and *j* started at 1.0 Å bond distance (*r*), then incrementally increased by 0.1 Å until *r*<sub>*ij*</sub> reached 4.0 Å. Each molecule was aligned in the *x-y* plane and the bonds between atoms *i* and *j* were aligned with the *x*-axis of the simulation cell, in order to easily increase the interatomic distance of atoms *i* and *j*. In total, we utilized 31 structures of the same molecule, each with a different bond length. At each bond distance, all atoms were frozen except for the atoms *i* and *j* involved in the bond to be dissociated. A geometry optimization (= energy minimization) was then performed using LAMMPS to obtain the respective energy. The energy from each molecule was then plotted vs the bond distance. The  $\alpha$  parameter and the bond dissociation energy *D* could then be tuned to match the MP2 or DFT results (Figure 2).

The quantum mechanical simulations were performed using the Gaussian 2016 software package.<sup>66</sup> The bond dissociation energies given by IFF-R and the ReaxFF parameter set developed by Singh et al. (ref. <sup>34</sup>) were compared to two methods of quantum mechanical calculations, DFT(B3LYP) and 2<sup>nd</sup> order Møller–Plesset perturbation theory (MP2). The spin-polarized calculations were performed using the Hartree-Fock theory together with MP2 and the B3LYP gradient-corrected hybrid DFT.<sup>67,68</sup> The standard split-valence polarized double-zeta basis sets 6-31G (d, p) was used for both DFT and MP2 calculations.<sup>69</sup> For quantum mechanical predictions, the fully-optimized molecular geometry was used to investigate the bond-breaking

process in which the bond length between atoms  $i$  and  $j$  were varied while freezing the remaining bonds in each molecule. These simulations were performed in vacuum at 0 K. The bond energy from each morphology was plotted vs bond distance to inform IFF-R and compare with ReaxFF predictions.

**4.2. Simulation of Tensile Modulus and Strength.** Molecular dynamics simulations of tensile loads simulations were performed by assigning Morse parameters to the bonds that experience uniaxial stress in the direction of deformation and were considered the relatively weakest according to their bond dissociation energies (for example, carbon-carbon single bonds). All other bonds were still assigned harmonic bond potentials. The Morse parameters for  $C_{ar}-C_{ar}$  partial double bonds were used for graphite and CNTs, the Morse parameters for C-C single bonds were used for PAN crystal, and no Morse bond parameters were needed for iron which does not involve bonded terms (only Lennard-Jones potentials). Morse bond parameters for cellulose included C-C single-bonds and C-O single bonds. The NVT ensemble was employed for the tensile simulations. During the simulation of tensile stress, the simulation box was expanded in the axial direction at a rate of  $2 \cdot 10^{-7}$  engineering strain every 10 timesteps. Each timestep was 0.5 femtoseconds and the simulations were run until material failure.

To calculate the Young's modulus (Table 1), the difference in the stress component associated with the axis of deformation was calculated at each timestep. For the stress calculation of the SWCNT simulation, the stress was normalized to account for cross-sectional area of the CNT and neglect the large amount of vacuum in the simulation box. The normalized area (in nm) was calculated using the equation  $A = N(\pi(r+0.19)^2)$ , where  $N$  is the number of CNTs and  $r$  is the initial radius of the CNT with the addition of a van-der-Waals correction of 0.19 nm (half of the graphite layer spacing). The strain was calculated by enumerating the change in box dimension

with respect to the original box dimension. The Young's modulus was calculated by applying a best fit line on the linear stress-strain response of the material (e.g. between 0.000 to 0.010 strain). The tensile strength was defined as the maximum stress before material failure.

For comparison, the SWCNT, PAN crystal, and cellulose I $\beta$  crystal the tensile simulations were also run using a ReaxFF parameter set developed by Liu et al., and a ReaxFF parameter set developed by Damirchi et al (Figure 4a-c). We note that the ReaxFF parameter sets used were not optimized for the simulated systems, however, they were chosen because of their capability of simulating systems containing carbon, hydrogen, oxygen, and nitrogen simultaneously.<sup>38, 63</sup> The ReaxFF parameter set used to compare the iron tensile simulation was developed by Islam et al for analyzing hydrogen embrittlement in pure and defective iron and may not accurately capture the phenomenon of tensile failure of a pure iron crystal.<sup>48</sup> However, the Islam ReaxFF parameters appeared to be the currently most relevant for the iron tensile simulation tests.

**4.3. Surface Energy of Graphite and  $\gamma$ -Iron (1 1 1).** To calculate the surface energy of graphite, a bulk graphitic structure was created with lattice parameters  $a = 1.476$  nm,  $b = 1.2874$  nm,  $c = 4.08$  nm, and  $\alpha=\beta=\gamma=90^\circ$ . The spacing between graphitic layers was 0.3685 nm, so that the density of the structure was calculated to be 2.164 g/cm<sup>3</sup>. A molecular dynamics simulation in the NPT ensemble was performed at 298 K and the equilibrated average total energy over 1 nanosecond was recorded, represented by  $E_{\text{bulk}}$  (eq 3). The equilibrated unit cell dimensions were noted and used to generate a new graphitic structure that had 12 nm of vacuum space between two graphitic slabs of equal dimensions, effectively creating two new graphitic surfaces. A subsequent MD simulation in the NPT ensemble was used to compute the average total energy of this system over 1 nanosecond, represented by  $E_{\text{slab}}$  (eq 3). From the energies of these two types of graphitic systems, the surface energy of graphite was determined using eq 3.

$$\gamma = \frac{E_{slab} - E_{bulk}}{2 \times A} \quad (2)$$

A similar procedure was used to find the surface energy of the (111)  $\gamma$ -iron surface. The bulk  $\gamma$ -iron lattice parameters were defined as  $a = 1.76505$  nm,  $b = 2.1837$  nm,  $c = 1.85295$  nm, and  $\alpha = \beta = \gamma = 90^\circ$ . A slab was created in which the two equal-dimension  $\gamma$ -iron slabs were separated by 10 nm of vacuum space, and subsequent average energies from MD simulations were used to calculate the surface energy.

**4.4. Calculation of Enthalpy of Vaporization and Sublimation of Molecules and Polymers.** The enthalpy of vaporization of propionitrile and enthalpy of sublimation of  $\alpha$ -D-glucose were calculated to validate the reproduction of energies for PAN and cellulose I $\beta$ , respectively, by the IFF-R Hamiltonian. The procedure involved creating liquid and gaseous simulation cells for the propionitrile, and a crystal and gaseous simulation cell for  $\alpha$ -D-glucose. The liquid propionitrile lattice dimensions were defined such that 108 propionitrile molecules fit into an orthogonal unit cell with dimensions  $a = 24.6$  Å,  $b = 24.0$  Å, and  $c = 24.48$  Å. The given dimensions reproduced propionitrile's experimentally determined density of 0.683 g/cm<sup>3</sup>. The vapor structure was an orthogonal simulation cell with lattice dimensions of  $a = b = c = 630$  Å and contained 20 propionitrile molecules.

The purpose of creating a large simulation cell was to make it unlikely for any of the molecules to interact with each other during the simulation. A model of the crystal structure of  $\alpha$ -D-glucose was created using unit cell dimensions measured by McDonald et al.<sup>70</sup> The final supercell of crystalline  $\alpha$ -D-glucose used contained 64 glucose molecules and had lattice parameters of  $a = 18.58$  Å,  $b = 25.30$  Å,  $c = 26.80$  Å. The simulation cell for  $\alpha$ -D-glucose in the vapor phase contained 20 glucose molecules and had lattice parameters of  $a = b = c = 1000$  Å. MD

simulations of liquid propionitrile and glucose crystals were run for 1 nanosecond (following longer initial equilibration) using the NPT ensemble. The vapor simulations were run for 1 nanosecond using the NVT ensemble. Equation 3 was used to calculate enthalpy for each material.

$$\Delta h_{v,s} = \langle E_{vap} \rangle - \langle E_{liq,cry} \rangle + RT \quad (3)$$

In eq. 3,  $\Delta h_{v,s}$  is enthalpy of vaporization or sublimation depending on the material,  $E_{vap}$  is the average molecular energy of the vapor simulation,  $E_{liq,cry}$  is the average molecular energy of the liquid or crystal simulation, and  $RT$  is the gas constant 8.314 J/mol multiplied by the simulation temperature (Table 2). All values were normalized per one mol of molecules.

**4.5. Uncertainties and Limitations.** Using the Morse bond parameters to dissociate bonds is a key first step to visualize and thermodynamically analyze failure in materials. It does not yet provide an adequate means of visualizing failure of polymers after initial bond dissociation using, for example, LAMMPS. There are workarounds to visualize complete bond dissociation in a polymer network and single polymer chains. However, we recommended a more comprehensive solution in the future that includes bond cutoffs, potentially the normalization of the Morse bond energy after dissociation to zero, as well as provisions for the formation of bonds, or reconstruction of chemical bonds. Clearly, such additions will increase the complexity of simulation algorithms yet are likely to add outstanding value.

Using an existing curve of harmonic bond energy vs bond distance, plus a target value for the bond dissociation energy is a good path to parameterize a new Morse bond potential. We recommend to use highly accurate experimental data and only high-level quantum mechanical methods, e.g., at least MP2, CCSD, and not plain DFT. Matching computed mechanical properties to experimental reference data can also help optimize Morse parameters for a specific chemical

species, if the composition and crystallinity are well-defined and accurately known. In addition, non-bonded forces may play an important role in the mechanical performance of some materials, for example, hydrogen bonding in cellulose and Kevlar. Artificially increasing the stiffness of a bond, for example by increasing the  $\alpha$  parameter, to match an experimentally determined Young's modulus and the ultimate strength can thus be a pitfall and could create non-physical Morse bond parameters. The definition via equilibrium bond length, vibration spectra, and accurate bond dissociation energies can be considered failsafe.

During the Morse bond parameterization, we observed that discrepancies in bonded parameters and in nonbonded parameters (charges, LJ parameters) in several existing parent force fields were not suitable for reproducing experimentally determined material properties (e.g. cellulose and glucose in PCFF). Such issues are avoided across the periodic table by following IFF protocol, which builds on complete physical interpretation and transferability. In particular, for systems with mechanical properties governed significantly by hydrogen bonding interactions it is strongly encouraged to ensure that bond parameters, angle parameters, torsions, charges, and LJ parameters can be reasonably validated and are capable to reproduce material properties in agreement with experimental or high-level quantum mechanical data (i.e. IFF standards) before developing Morse bond parameters (e.g., IFF-R). We also note that quantum mechanical simulations, especially at the DFT level, can have high errors, and should be avoided whenever reproducible experimental information is available.

**4.5. Availability of Tutorials and Code.** A first tutorial explaining the concept of IFF-R and initial examples including code has been available on our website since January 2020 (<https://bionanostructures.com/interface-md/>).

## Acknowledgements

This work was supported by NASA (STRI NNX17AJ32G), the National Science Foundation (CMMI 1940335, OAC 1931587), and the University of Colorado at Boulder. We acknowledge the allocation of computational resources at the Summit supercomputer, a joint effort of the University of Colorado Boulder and Colorado State University, which is supported by the National Science Foundation (ACI-1532235 and ACI-1532236), and resources at the Argonne Leadership Computing Facility, which is a DoE Office of Science User Facility supported under Contract DE-AC02-06CH11357.

**Supporting Information Available:** Supporting files with additional figures. Models, simulation scripts, and a tutorial on using IFF-R are available online (<https://bionanostructures.com/interface-md/>).

**Conflict of Interest:** The authors declare no conflicts of interest.

## References

1. Liu, Z. Q.; Zhang, Z. F.; Ritchie, R. O., Structural Orientation and Anisotropy in Biological Materials: Functional Designs and Mechanics. *Adv. Funct. Mater.* **2020**, *30* (10), 1908121.
2. Ling, S. J.; Kaplan, D. L.; Buehler, M. J., Nanofibrils in Nature and Materials Engineering. *Nat. Rev. Mater.* **2018**, *3* (4), 18016.
3. Chang, H.; Luo, J.; Gulgunje, P. V.; Kumar, S., Structural and Functional Fibers. *Ann. Rev. Mater. Res.* **2017**, *47* (13), 13.1-13.29.
4. Heinz, H.; Lin, T. J.; Mishra, R. K.; Emami, F. S., Thermodynamically Consistent Force Fields for the Assembly of Inorganic, Organic, and Biological Nanostructures: The INTERFACE Force Field. *Langmuir* **2013**, *29* (6), 1754-1765.

5. Lindorff-Larsen, K.; Piana, S.; Dror, R. O.; Shaw, D. E., How Fast-Folding Proteins Fold. *Science* **2011**, *334* (6055), 517-520.
6. Heinz, H.; Ramezani-Dakhel, H., Simulations of Inorganic–Bioorganic Interfaces to Discover New Materials: Insights, Comparisons to Experiment, Challenges, and Opportunities. *Chem. Soc. Rev.* **2016**, *45* (2), 412-448.
7. Pisani, W. A.; Radue, M. S.; Chinkanjanarot, S.; Bednarczyk, B. A.; Pineda, E. J.; Waters, K.; Pandey, R.; King, J. A.; Odegard, G. M., Multiscale Modeling of PEEK Using Reactive Molecular Dynamics Modeling and Micromechanics. *Polymer* **2019**, *163*, 96-105.
8. Ruan, L. Y.; Ramezani-Dakhel, H.; Lee, C.; Li, Y. J.; Duan, X. F.; Heinz, H.; Huang, Y., A Rational Biomimetic Approach to Structure Defect Generation in Colloidal Nanocrystals. *ACS Nano* **2014**, *8* (7), 6934-6944.
9. Kanhaiya, K.; Kim, S.; Im, W.; Heinz, H., Accurate Simulation of Surfaces and Interfaces of Ten FCC Metals and Steel Using Lennard–Jones Potentials. *npj Comput. Mater.* **2021**, *7* (1), 17.
10. Jamil, T.; Javadi, A.; Heinz, H., Mechanism of Molecular Interaction of Acrylate-Polyethylene Glycol Acrylate Copolymers with Calcium Silicate Hydrate Surfaces. *Green Chemistry* **2020**, *22* (5), 1577-1593.
11. Gissinger, J. R.; Pramanik, C.; Newcomb, B.; Kumar, S.; Heinz, H., Nanoscale Structure-Property Relationships of Polyacrylonitrile/CNT Composites as a Function of Polymer Crystallinity and CNT Diameter. *ACS Appl. Mater. Interfaces* **2018**, *10* (1), 1017-1027.
12. MacKerell, A. D.; Bashford, D.; Bellott, M.; Dunbrack, R. L.; Evanseck, J. D.; Field, M. J.; Fischer, S.; Gao, J.; Guo, H.; Ha, S.; Joseph-McCarthy, D.; Kuchnir, L.; Kuczera, K.; Lau, F. T. K.; Mattos, C.; Michnick, S.; Ngo, T.; Nguyen, D. T.; Prodhom, B.; Reiher, W. E.; Roux, B.; Schlenkrich, M.; Smith, J. C.; Stote, R.; Straub, J.; Watanabe, M.; Wiorkiewicz-Kuczera, J.; Yin, D.; Karplus, M., All-atom empirical potential for molecular modeling and dynamics studies of proteins. *J Phys Chem B* **1998**, *102* (18), 3586-3616.
13. Sauer, J., Ab Initio Calculations for Molecule-Surface Interactions with Chemical Accuracy. *Acc. Chem. Res.* **2019**, *52* (12), 3502-3510.
14. Ruiz, V. G.; Liu, W.; Tkatchenko, A., Density-Functional Theory with Screened van der Waals Interactions Applied to Atomic and Molecular Adsorbates on Close-Packed and Non-Close-Packed Surfaces. *Phys. Rev. B* **2016**, *93* (3), 035118.
15. Goerigk, L.; Grimme, S., A Thorough Benchmark of Density Functional Methods for General Main Group Thermochemistry, Kinetics, and Noncovalent Interactions. *Phys. Chem. Chem. Phys.* **2011**, *13* (14), 6670-6688.
16. Dharmawardhana, C. C.; Kanhaiya, K.; Lin, T. J.; Garley, A.; Knecht, M. R.; Zhou, J. H.; Miao, J. W.; Heinz, H., Reliable computational design of biological-inorganic materials to the large nanometer scale using Interface-FF. *Mol Simulat* **2017**, *43* (13-16), 1394-1405.
17. Pramanik, C.; Nepal, D.; Nathanson, M.; Gissinger, J. R.; Garley, A.; Berry, R. J.; Davijani, A.; Kumar, S.; Heinz, H., Molecular engineering of interphases in polymer/carbon nanotube composites to reach the limits of mechanical performance. *Compos Sci Technol* **2018**, *166*, 86-94.
18. van Duin, A. C. T.; Dasgupta, S.; Lorant, F.; Goddard, W. A., ReaxFF: A reactive force field for hydrocarbons. *J Phys Chem A* **2001**, *105* (41), 9396-9409.
19. Lide, D. R., *CRC Handbook of Chemistry and Physics* 96th ed.; CRC Press: Boca Raton, FL, 2015.
20. Blanksby, S. J.; Ellison, G. B., Bond Dissociation Energies of Organic Molecules. *Acc. Chem. Res.* **2003**, *36* (4), 255-263.

21. Darwent, B. D., Bond Dissociation Energies in Simple Molecules. *Nat. Stand. Ref. Data Ser., Nat. Bur. Stand. (U. S.)* **1970**, 31, NSRDS-NBS 31.
22. *NIST Chemistry WebBook*. US Department of Commerce: DOI: doi.org/10.18434/T4D303, 2018.
23. St John, P. C.; Guan, Y. F.; Kim, Y.; Kim, S.; Paton, R. S., Prediction of Organic Homolytic Bond Dissociation Enthalpies at Near Chemical Accuracy with Sub-Second Computational Cost. *Nat. Commun.* **2020**, 11 (1), 2328.
24. Dauberosguthorpe, P.; Roberts, V. A.; Osguthorpe, D. J.; Wolff, J.; Genest, M.; Hagler, A. T., Structure and Energetics of Ligand-Binding to Proteins - Escherichia-Coli Dihydrofolate Reductase Trimethoprim, a Drug-Receptor System. *Proteins-Structure Function and Genetics* **1988**, 4 (1), 31-47.
25. Heinz, H.; Koerner, H.; Anderson, K. L.; Vaia, R. A.; Farmer, B. L., Force Field for Mica-Type Silicates and Dynamics of Octadecylammonium Chains Grafted to Montmorillonite. *Chem. Mater.* **2005**, 17 (23), 5658-5669.
26. Pramanik, C.; Gissinger, J. R.; Kumar, S.; Heinz, H., Carbon Nanotube Dispersion in Solvents and Polymer Solutions: Mechanisms, Assembly, and Preferences. *Acs Nano* **2017**, 11 (12), 12805-12816.
27. Tersoff, J., Empirical Interatomic Potential for Silicon with Improved Elastic Properties. *Phys Rev B* **1988**, 38 (14), 9902-9905.
28. Stuart, S. J.; Tutein, A. B.; Harrison, J. A., A reactive potential for hydrocarbons with intermolecular interactions. *J Chem Phys* **2000**, 112 (14), 6472-6486.
29. Zavitsas, A. A., The Relation between Bond Lengths and Dissociation Energies of Carbon-Carbon Bonds. *J. Phys. Chem. A* **2003**, 107 (6), 897-898.
30. Zeinalipour-Yazdi, C. D.; Loizidou, E. Z.; Chutia, A., Size-Dependent Bond Dissociation Enthalpies in Single-Walled Carbon Nanotubes. *Chem. Phys. Lett.* **2019**, 731, 136628.
31. Plimpton, S., Fast Parallel Algorithms for Short-Range Molecular Dynamics. *J. Comput. Phys.* **1995**, 117 (1), 1-19.
32. Wang, S.; Liang, R.; Wang, B.; Zhang, C., Covalent addition of diethyltoluenediamines onto carbon nanotubes for composite application. *Polym Composite* **2009**, 30 (8), 1050-1057.
33. Xie, H.; Liu, B.; Yang, H.; Wang, Z.; Shen, J.; Cheng, R., Thermal characterization of carbon-nanofiber-reinforced tetraglycidyl-4,4'-diaminodiphenylmethane/4,4'-diaminodiphenylsulfone epoxy composites. *J Appl Polym Sci* **2006**, 100 (1), 295-298.
34. Singh, S. K.; Srinivasan, S. G.; Neek-Amal, M.; Costamagna, S.; van Duin, A. C. T.; Peeters, F. M., Thermal properties of fluorinated graphene. *Phys Rev B* **2013**, 87 (10).
35. Smith, M. B., *March's Advanced Organic Chemistry: Reactions, Mechanism, and Structure*. 7th ed.; Wiley: Hoboken, NJ, 2013.
36. Bai, Y. X.; Zhang, R. F.; Ye, X.; Zhu, Z. X.; Xie, H. H.; Shen, B. Y.; Cai, D. L.; Liu, B. F.; Zhang, C. X.; Jia, Z.; Zhang, S. L.; Li, X. D.; Wei, F., Carbon nanotube bundles with tensile strength over 80 GPa. *Nat Nanotechnol* **2018**, 13 (7), 589-+.
37. Nishiyama, Y.; Langan, P.; Chanzy, H., Crystal structure and hydrogen-bonding system in cellulose 1 beta from synchrotron X-ray and neutron fiber diffraction. *J Am Chem Soc* **2002**, 124 (31), 9074-9082.
38. Liu, L. C.; Liu, Y.; Zybin, S. V.; Sun, H.; Goddard, W. A., ReaxFF-/g: Correction of the ReaxFF Reactive Force Field for London Dispersion, with Applications to the Equations of State for Energetic Materials. *J Phys Chem A* **2011**, 115 (40), 11016-11022.

39. Damirchi, B.; van Duin, A., Computational investigation on carbon nanotube-composite interactions using the ReaxFF reactive force field. *Abstr Pap Am Chem S* **2019**, 257.
40. Islam, M. M.; Zou, C.; van Duin, A. C. T.; Raman, S., Interactions of hydrogen with the iron and iron carbide interfaces: a ReaxFF molecular dynamics study. *Phys Chem Chem Phys* **2016**, *18* (2), 761-771.
41. Kanski, M.; Maciazek, D.; Postawa, Z.; Ashraf, C. M.; van Duin, A. C. T.; Garrison, B. J., Development of a Charge-Implicit ReaxFF Potential for Hydrocarbon Systems. *J Phys Chem Lett* **2018**, *9* (2), 359-363.
42. Strachan, A.; van Duin, A. C. T.; Chakraborty, D.; Dasgupta, S.; Goddard, W. A., Shock waves in high-energy materials: The initial chemical events in nitramine RDX. *Phys Rev Lett* **2003**, *91* (9).
43. Chenoweth, K.; van Duin, A. C. T.; Goddard, W. A., ReaxFF reactive force field for molecular dynamics simulations of hydrocarbon oxidation. *J Phys Chem A* **2008**, *112* (5), 1040-1053.
44. Zhang, R. F.; Wen, Q.; Qian, W. Z.; Su, D. S.; Zhang, Q.; Wei, F., Superstrong Ultra long Carbon Nanotubes for Mechanical Energy Storage. *Adv Mater* **2011**, *23* (30), 3387-+.
45. Zhang, R. F.; Zhang, Y. Y.; Wei, F., Controlled Synthesis of Ultralong Carbon Nanotubes with Perfect Structures and Extraordinary Properties. *Accounts Chem Res* **2017**, *50* (2), 179-189.
46. Zhao, Q. Z.; Nardelli, M. B.; Bernholc, J., Ultimate strength of carbon nanotubes: A theoretical study. *Phys Rev B* **2002**, *65* (14).
47. Clark, S. J.; Segall, M. D.; Pickard, C. J.; Hasnip, P. J.; Probert, M. J.; Refson, K.; Payne, M. C., First principles methods using CASTEP. *Z Kristallogr* **2005**, *220* (5-6), 567-570.
48. Islam, M. M.; Zou, C. Y.; van Duin, A. C. T.; Raman, S., Interactions of hydrogen with the iron and iron carbide interfaces: a ReaxFF molecular dynamics study. *Phys Chem Chem Phys* **2016**, *18* (2), 761-771.
49. Iwamoto, S.; Kai, W. H.; Isogai, A.; Iwata, T., Elastic Modulus of Single Cellulose Microfibrils from Tunicate Measured by Atomic Force Microscopy. *Biomacromolecules* **2009**, *10* (9), 2571-2576.
50. Moon, R. J.; Martini, A.; Nairn, J.; Simonsen, J.; Youngblood, J., Cellulose nanomaterials review: structure, properties and nanocomposites. *Chem Soc Rev* **2011**, *40* (7), 3941-3994.
51. Benito, J. A.; Manero, J. M.; Jorba, J.; Roca, A., Change of Young's modulus of cold-deformed pure iron in a tensile test. *Metall Mater Trans A* **2005**, *36A* (12), 3317-3324.
52. Brenner, S. S., Tensile Strength of Whiskers. *J Appl Phys* **1956**, *27* (12), 1484-1491.
53. Zacharia, R.; Ulbricht, H.; Hertel, T., Interlayer cohesive energy of graphite from thermal desorption of polyaromatic hydrocarbons. *Phys Rev B* **2004**, *69* (15).
54. Liu, Z.; Liu, J. Z.; Cheng, Y.; Li, Z. H.; Wang, L.; Zheng, Q. S., Interlayer binding energy of graphite: A mesoscopic determination from deformation. *Phys Rev B* **2012**, *85* (20).
55. Shih, C. J.; Strano, M. S.; Blankschtein, D., Wetting translucency of graphene. *Nat Mater* **2013**, *12* (10), 866-869.
56. Tyson, W. R.; Miller, W. A., Surface Free-Energies of Solid Metals - Estimation from Liquid Surface-Tension Measurements. *Surf Sci* **1977**, *62* (1), 267-276.
57. Roth, T. A., Determination of the Surface and Grain-Boundary Free-Energies of Titanium-Alloys Having a Bamboo Structure. *Jom-J Min Met Mat S* **1985**, *37* (8), A65-A65.
58. Spencer, M. J. S.; Hung, A.; Snook, I. K.; Yarovsky, I., Density functional theory study of the relaxation and energy of iron surfaces. *Surf Sci* **2002**, *513* (2), 389-398.

59. Shin, Y. K.; Gai, L. L.; Raman, S.; van Duin, A. C. T., Development of a ReaxFF Reactive Force Field for the Pt-Ni Alloy Catalyst. *J Phys Chem A* **2016**, *120* (41), 8044-8055.
60. Linstrom, P. J.; Mallard, W. G., The NIST Chemistry WebBook: A chemical data resource on the internet. *J Chem Eng Data* **2001**, *46* (5), 1059-1063.
61. Weber, L. A.; Kilpatrick, J. E., Entropy and Related Thermodynamic Properties of Propionitrile. *J Chem Phys* **1962**, *36* (3), 829-&.
62. Oja, V.; Suuberg, E. M., Vapor pressures and enthalpies of sublimation of D-glucose, D-xylose, cellobiose, and levoglucosan. *J Chem Eng Data* **1999**, *44* (1), 26-29.
63. Damirchi, B.; Radue, M.; Kanhaiya, K.; Heinz, H.; Odegard, G. M.; van Duin, A. C. T., ReaxFF Reactive Force Field Study of Polymerization of a Polymer Matrix in a Carbon Nanotube-Composite System. *J Phys Chem C* **2020**, *124* (37), 20488-20497.
64. Dauber-Osguthorpe, P.; Roberts, V. A.; Osguthorpe, D. J.; Wolff, J.; Genest, M.; Hagler, A. T., Structure and Energetics of Ligand Binding to Proteins: Escherichia Coli Dihydrofolate Reductase-Trimethoprim, a Drug-Receptor System. *Proteins: Struct., Funct., Genet.* **1988**, *4* (1), 31-47.
65. *Materials Studio 2019 Program Suite and User Guide*. Biovia/Dassault Systemes: Cambridge, UK, 2019.
66. Frisch, M. J.; Trucks, G. W.; Schlegel, H. B.; Scuseria, G. E.; Robb, M. A.; Cheeseman, J. R.; Scalmani, G.; Barone, V.; Petersson, G. A.; Nakatsuji, H.; Li, X.; Caricato, M.; Marenich, A. V.; Bloino, J.; Janesko, B. G.; Gomperts, R.; Mennucci, B.; Hratchian, H. P.; Ortiz, J. V.; Izmaylov, A. F.; Sonnenberg, J. L.; Williams; Ding, F.; Lipparini, F.; Egidi, F.; Goings, J.; Peng, B.; Petrone, A.; Henderson, T.; Ranasinghe, D.; Zakrzewski, V. G.; Gao, J.; Rega, N.; Zheng, G.; Liang, W.; Hada, M.; Ehara, M.; Toyota, K.; Fukuda, R.; Hasegawa, J.; Ishida, M.; Nakajima, T.; Honda, Y.; Kitao, O.; Nakai, H.; Vreven, T.; Throssell, K.; Montgomery Jr., J. A.; Peralta, J. E.; Ogliaro, F.; Bearpark, M. J.; Heyd, J. J.; Brothers, E. N.; Kudin, K. N.; Staroverov, V. N.; Keith, T. A.; Kobayashi, R.; Normand, J.; Raghavachari, K.; Rendell, A. P.; Burant, J. C.; Iyengar, S. S.; Tomasi, J.; Cossi, M.; Millam, J. M.; Klene, M.; Adamo, C.; Cammi, R.; Ochterski, J. W.; Martin, R. L.; Morokuma, K.; Farkas, O.; Foresman, J. B.; Fox, D. J. *Gaussian 16 Rev. C.01*, Wallingford, CT, 2016.
67. Pople, J. A.; Binkley, J. S.; Seeger, R., Theoretical Models Incorporating Electron Correlation. *Int J Quantum Chem* **1976**, 1-19.
68. Becke, A. D., A New Mixing of Hartree-Fock and Local Density-Functional Theories. *J Chem Phys* **1993**, *98* (2), 1372-1377.
69. Hehre, W. J.; Ditchfield, R.; Pople, J. A., Self-Consistent Molecular-Orbital Methods .12. Further Extensions of Gaussian-Type Basis Sets for Use in Molecular-Orbital Studies of Organic-Molecules. *J Chem Phys* **1972**, *56* (5), 2257-+.
70. McDonald, T. R. R.; Beevers, C. A., The Crystal and Molecular Structure of Alpha-Glucose. *Acta Crystallogr* **1952**, *5* (5), 654-659.

## Supporting Information

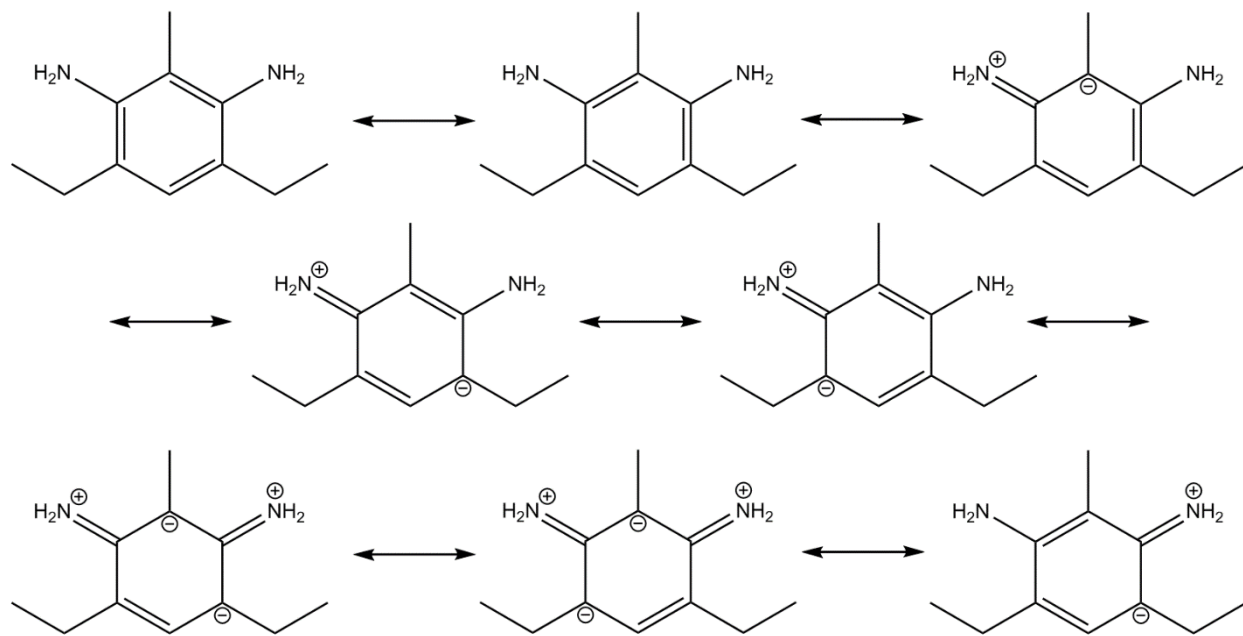
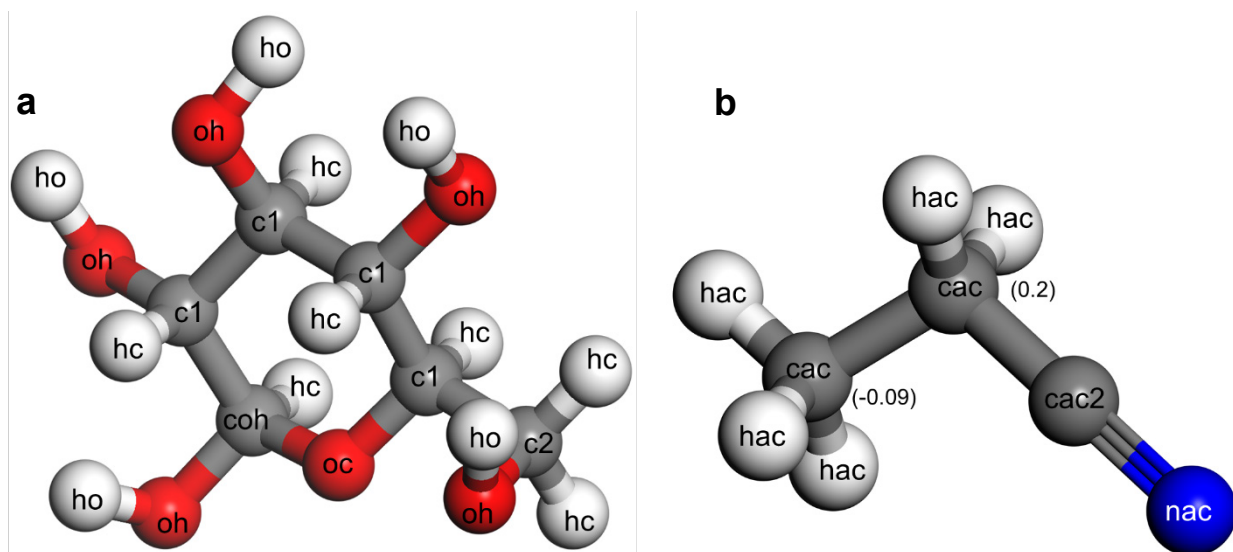


**Figure S1.** Resonance structures of DETDA, showing increasing double bond character in the order 2, 3 < 1, 2 < 3, 4.



**c**

Atom type	9-6 Lennard-Jones potential		Atomic charge (e)
	Sigma	Epsilon	
ho	1.098	0.013	0.45
hc	2.7	0.02	0.03
oh	3.4	0.28	-0.7
oc	3.4	0.18	-0.5
coh	4.0	0.05	0.47
c1	4.0	0.06	0.22
c2	4.0	0.06	0.19
hac	3.0	0.02	0.03
cac	4.0	0.06	-0.09/0.30
cac2	4.0	0.05	0.35
nac	4.1	0.24	-0.71

**Figure S2.** (a, b) Glucose and propionitrile structures with atom types (force field types) indicated. The model of propionitrile also lists the charges on the carbon backbone. (c) Table of force field types, atomic charges, and non-bond parameters. The parameters for propionitrile are IFF-R and the parameters for glucose are PCFF-R including updated atomic charges.